

# Dark matter trio in classically conformal theories: WIMP, supercooling, and monopole

Ke-Pan Xie<sup>1,\*</sup> and Cheng-Hao Zhan<sup>1,†</sup>

<sup>1</sup>*School of Physics, Beihang University, Beijing 100191, China*

Beyond solving the hierarchy problem, classically conformal (CC) theories naturally accommodate dark matter (DM). In this work, we explore the CC  $SU(2)_X$  gauge theory with a triplet dark scalar, uncovering three distinct DM scenarios: WIMP, supercooled DM, and monopole. The production mechanisms are strongly influenced by the CC model's unique first-order phase transition evolution history, which differs significantly from those in non-conformal models. We obtain the viable parameter space for each scenario and investigate the current constraints and future sensitivities at terrestrial experiments and gravitational wave observatories.

## I. INTRODUCTION

As the only elementary scalar in the Standard Model (SM), the Higgs boson suffers from the quadratic divergence in its self-energy from quantum corrections at high scales, known as the gauge hierarchy problem [1]. A promising solution is the classically conformal (CC) principle [2, 3], where the theory contains no dimensionful parameters at tree level, preserving conformal invariance. The conformal symmetry is then broken radiatively via the Coleman-Weinberg (CW) potential [4, 5], dynamically generating the scale. Given the observed Higgs mass  $m_h \approx 125$  GeV [6], a viable realization of this idea is to first trigger conformal symmetry breaking in a hidden sector through the CW mechanism, and then transmit it partially to the SM electroweak (EW) sector via Higgs portal interactions [7–13].

Beyond the particle physics motivation, CC theories also offer solutions to puzzles in cosmology, such as dark matter (DM), which contributes  $\sim 26\%$  to the total energy of the Universe [14]. An appealing minimal DM scenario within this framework is a gauged hidden sector, where the new gauge boson plays a dual role: it generates a CW potential for the dark scalar to break the conformal and gauge symmetries, and it serves as a vector DM candidate. Previous studies have explored this scenario for a  $U(1)_X$  group [15–18] and for an  $SU(2)_X$  group with the dark scalar in the fundamental representation [18–22].

In this research, we investigate the DM scenario within a CC  $SU(2)_X$  theory, featuring a dark scalar  $\phi$  in the adjoint representation. The non-Abelian nature of the dark gauge group prevents any kinetic mixing with the SM hypercharge  $U(1)_Y$ , thereby ensuring the stability of the vector DM candidate. Moreover, a triplet  $\phi$  induces the symmetry-breaking pattern  $SU(2)_X \rightarrow U(1)_X$ , and this residual unbroken group guarantees the absolute stability of vector DM. This is different from scenarios where the dark scalar is a doublet; in those models,  $SU(2)_X$  is completely broken, and non-renormalizable operators can mediate DM decay to the SM particles [23]. An additional feature of the triplet scenario is the existence of a topological soliton, i.e., the 't Hooft-Polyakov monopole [24, 25], offering an extra DM candidate.

DM within non-conformal  $SU(2)_X$  theories has been studied extensively, with the dark scalar in the fundamental [23, 26–28], adjoint [29–34], or higher representations [35–37]. In those models, tree-level mass parameters trigger the  $SU(2)_X$  and EW symmetries breaking, and the cosmological evolution typically follows a standard adiabatic thermal history, leading to freeze-out of the weakly interacting massive particle (WIMP) DM. The CC framework in the current paper differs in two crucial aspects as follows.

First, symmetry breaking in CC theories is driven by radiative corrections, resulting in a more predictive scenario with fewer free parameters. Second, as first proposed by Witten [38] and now actively studied [39–51], the CC theories usually feature a supercooled first-order phase transition (FOPT), which could significantly impact the cosmological history and formation of DM [19, 20, 52–57] or primordial black holes [58–64], as well as the generation of the baryon asymmetry [65–67].

In this work, we identify three distinct DM scenarios within the CC  $SU(2)_X$  model with a triplet scalar: (i) the dark gauge boson  $X$  as a WIMP via the conventional freeze-out mechanism; (ii) supercooled DM, where an ultra-supercooled FOPT leads to dilution and nonthermal production of  $X$  after the transition [19, 20, 54, 55]; and (iii) monopole DM arising from bubble nucleation dynamics. For each case, we identify the parameter space that explains the full DM relic abundance and explore its phenomenological signatures.

This paper is organized as follows. In Section II, we introduce the model Lagrangian and derive the particle spectrum. Section III then describes the unique cosmological thermal history in this model, which distinguishes the CC theory from non-conformal models. The three DM scenarios are detailed in Section IV, while the DM parameter space and the corresponding phenomenological analysis are presented in Section V. We conclude in Section VI.

## II. THE MODEL

The hidden sector is gauged under a dark  $SU(2)_X$ , and  $X_\mu^a = (X_\mu^1, X_\mu^2, X_\mu^3)$  is the corresponding gauge field. We introduce the real scalar  $\phi_a = (G_1, G_2, s)^T$ , which is a triplet under  $SU(2)_X$  and a singlet under the SM gauge group  $SU(2)_L \times U(1)_Y$ . The Lagrangian is

$$\mathcal{L} \supset -\frac{1}{4}X_{\mu\nu}^a X_a^{\mu\nu} + \frac{1}{2}D_\mu\phi^a D^\mu\phi^a - V_0(\phi, H), \quad (1)$$

\* kpxie@buaa.edu.cn

† chzhan@buaa.edu.cn

where the dark covariant derivative is

$$(D_\mu \phi)_a = \partial_\mu \phi_a + g_X \epsilon^{abc} X_\mu^b \phi_c, \quad (2)$$

with  $g_X$  being the dark gauge coupling, and the field strength tensor is

$$X_{\mu\nu}^a = \partial_\mu X_\nu^a - \partial_\nu X_\mu^a + g_X \epsilon^{abc} X_\mu^b X_\nu^c, \quad (3)$$

with  $\epsilon^{abc}$  being the 3-dimensional Levi-Civita tensor under the convention  $\epsilon^{123} = 1$ .

The tree-level joint potential for  $\phi$  and the SM Higgs doublet  $H = (G^+, (h + iG^0)/\sqrt{2})^T$  reads

$$V(H, \phi) = \lambda_h |H|^4 + \frac{\lambda_s}{4} (\phi^T \phi)^2 + \frac{\lambda_{hs}}{2} |H|^2 (\phi^T \phi), \quad (4)$$

which contains only dimensionless parameters. Consequently, all symmetries, including conformal invariance,  $SU(2)_X$ , and  $SU(2)_L \times U(1)_Y$ , are preserved at this order. However, radiative corrections change this picture. Working in the unitary gauge,  $H \rightarrow (0, h/\sqrt{2})^T$  and  $\phi \rightarrow (0, 0, s)^T$ , and assuming the  $SU(2)_X$  scale  $\langle s \rangle = w$  much higher than the EW scale  $\langle h \rangle = v = 246$  GeV, we can adopt the sequential symmetry breaking approximation [68]. In this limit, the one-loop potential is

$$V_1(h, s) = \frac{3g_X^4}{16\pi^2} s^4 \left( \log \frac{s}{w_0} - \frac{1}{4} \right) + \frac{\lambda_{hs}}{4} h^2 s^2 + \frac{\lambda_h}{4} h^4. \quad (5)$$

The logarithmic potential along the  $s$  direction is generated by  $X_\mu^a$  via the CW mechanism, yielding the vacuum expectation value (VEV)  $w \approx w_0$ . This breaks the conformal symmetry, and also breaks  $SU(2)_X$  down to  $U(1)_X$ , giving a mass  $m_X = g_X w$  to  $X_\mu/X_\mu^\dagger = (X_\mu^1 \pm iX_\mu^2)/\sqrt{2}$ , while  $X_\mu^3$  remains massless, denoted as the dark photon  $A'_\mu$ . Note  $X_\mu/X_\mu^\dagger$  is charged  $\mp 1$  under  $U(1)_X$  but neutral under the SM gauge group. The physical scalar  $s$  also acquires a mass  $m_s \approx \sqrt{3}g_X^2 w/(2\pi)$ . Following the  $SU(2)_X$  breaking, the negative portal coupling  $\lambda_{hs} \approx -m_h^2/w^2$  induces a negative mass-squared term  $-m_h^2 h^2/4$  for the Higgs field, triggering the EW symmetry breaking.

The portal coupling  $\lambda_{hs}$  also causes the mixing between the physical scalar bosons  $s$  and  $h$ , described by

$$\begin{pmatrix} h \\ s \end{pmatrix} \xrightarrow[\text{eigenstates}]{\text{to mass}} U \begin{pmatrix} h \\ s \end{pmatrix}, \quad U = \begin{pmatrix} \cos \theta & \sin \theta \\ -\sin \theta & \cos \theta \end{pmatrix}, \quad (6)$$

with  $|\theta| < \pi/4$  being the mixing angle that is fully determined by the potential in Eq. (5) [50]. Given the measured values of Higgs VEV  $v$  and mass  $m_h$ , our model possesses only two free parameters, which we choose as the mass eigenvalues  $m_X$  and  $m_s$  that are closely related to DM phenomenology. All other parameters, such as  $g_X$ ,  $w$  (or  $w_0$ ), and  $\theta$ , can then be derived analytically. Following the procedure outlined in Ref. [50], we obtain

$$w = \frac{1}{2\sqrt{2}\pi m_h m_s} \sqrt{\mathcal{D} \pm \sqrt{\mathcal{D}^2 - 36m_h^2 m_s^2 m_X^8}}. \quad (7)$$

for  $m_s \leq m_h$ , where  $\mathcal{D} = 3m_X^4 (m_h^2 + m_s^2) - 4\pi^2 m_h^2 m_s^2 v^2$ . A physical solution for  $w$  exists only if

$$m_X > \sqrt{\frac{2\pi m_h m_s v}{\sqrt{3}|m_s - m_h|}}, \quad (8)$$

which represents an implicit consistency condition in the  $(m_X, m_s)$  parameter space. Once  $w$  is determined,  $g_X = m_X/w$  is also derived, and  $\theta$  can be resolved from the relation

$$w = \frac{m_h^2 \cot \theta + m_s^2 \tan \theta}{|m_h^2 - m_s^2|} v. \quad (9)$$

This simplifies to  $\tan \theta \approx (v/w)m_h^2/(m_h^2 - m_s^2)$  for  $w \gg v$  [9]. Further details of this parametrization are provided in Appendix A.

After symmetry breaking, expanding the Lagrangian in Eq. (1) yields the interactions among the physical particles. The triple couplings are

$$\begin{aligned} \mathcal{L}_3 \supset & \frac{2m_X^2}{w} s X_\mu^\dagger X^\mu + i g_X (X_{\mu\nu}^\dagger X^\mu - X_{\mu\nu} X^{\dagger\mu}) A'^\nu \\ & + i g_X \partial^\mu A'^\nu (X_\mu^\dagger X_\nu - X_\mu X_\nu^\dagger), \end{aligned} \quad (10)$$

and the quartic couplings are

$$\begin{aligned} \mathcal{L}_4 \supset & g_X^2 s^2 X_\mu^\dagger X^\mu + g_X^2 (X^{\dagger\mu} X^\nu A'_\mu A'_\nu - X_\mu^\dagger X^\mu A'_\nu A'^\nu) \\ & + \frac{g_X^2}{2} (X_\mu^\dagger X_\nu X^{\dagger\mu} X^\nu - X_\mu^\dagger X^\mu X_\nu^\dagger X^\nu). \end{aligned} \quad (11)$$

The scalar boson  $s$  also couples to SM fermions and gauge bosons via the mixing angle  $\theta$ , and conversely, the Higgs boson  $h$  couples to  $X$  via the same mixing. The vertices between  $h$  and  $s$  are less relevant to DM dynamics and hence listed in Appendix A.

At tree-level,  $s$  does not couple to the dark photon because it is neutral under  $U(1)_X$ ; however, loop corrections involving the charged  $X$ -bosons generate the dimension-five operator

$$\mathcal{L}_{sA'A'} \approx \frac{7g_X^3}{32\pi^2 m_X} s F'_{\mu\nu} F'^{\mu\nu}, \quad (12)$$

with  $F'_{\mu\nu} \equiv \partial_\mu A'_\nu - \partial_\nu A'_\mu$ , thereby inducing the  $sA'A'$  coupling. This is analogous to the  $W$ -loop-induced Higgs-photon coupling  $hF_{\mu\nu}F^{\mu\nu}$  in the SM.

### III. THERMAL HISTORY

In the early Universe, the plasma induces a temperature dependence in the scalar potential. This usually leads to symmetry restoration at high temperatures and symmetry breaking at lower temperatures, thus driving a cosmic phase transition [69]. A distinguishing feature of CC theories is that they generally result in FOPTs.

### A. Classification of the evolution patterns

Because of the smallness of  $|\lambda_{hs}|$ , the thermal corrections of the dark and SM sectors can be treated separately. The finite-temperature effective potential is therefore

$$V_T(h, s, T) = V_1(h, s) + V_X^T(s, T) + V_h^T(h, T). \quad (13)$$

The full expression of  $V_T(h, s, T)$  is given in Appendix B by the standard finite-temperature quantum field theory; here, for illustration, we expand the thermal potential near the origin  $(h, s) = (0, 0)$ , which yields

$$\text{Eq. (13)} \approx V_1(h, s) + \frac{g_X^2 T^2}{4} \left(1 - \frac{g_X}{\pi}\right) s^2 + \frac{c_h T^2}{2} h^2, \quad (14)$$

where  $c_h = (3g^2 + g'^2)/16 + y_t^2/4 + \lambda_h/2 \approx 0.4$ . The CC potential  $V_1(h, s)$  is flat at the origin: both the first and second order derivatives vanish. Consequently, the  $T^2$ -terms always form a local minimum at  $(0, 0)$ , in which the Universe stays when  $T \gg w$ . As  $T$  drops to the critical temperature  $T_c$  (which is typically  $\lesssim w$ ), a global minimum (the true vacuum) exists at  $h, s \neq 0$ , which eventually aligns with the zero-temperature VEV  $(v, w)$ . However, as the origin remains a local minimum, a smooth transition to the true vacuum is forbidden. Instead, the Universe has to tunnel discontinuously to the true vacuum, yielding a FOPT.

The cosmic evolution is governed primarily by the FOPT dynamics of the high-scale sector [42]. We therefore focus on the  $O(3)$ -symmetric bounce solution action  $S_3/T$  derived from the  $s$ -direction thermal potential

$$V_T(s, T) = V_1(0, s) + V_X^T(s, T), \quad (15)$$

which determines the vacuum tunneling rate from  $s = 0$  to  $s \neq 0$  per unit volume as [70]

$$\Gamma(T) \sim T^4 \left( \frac{S_3}{2\pi T} \right)^{3/2} e^{-S_3/T}. \quad (16)$$

This leads to the nucleation of bubbles containing the true vacuum, resulting in a decreasing volume fraction  $F(T) = e^{-I(T)}$  of the false vacuum as  $T$  decreases, where [71, 72]

$$I(T) = \frac{4\pi}{3} \int_T^{T_c} \frac{\Gamma(T') dT'}{T'^4 H(T')} \left( \int_T^{T'} \frac{v_w dT''}{H(T'')} \right)^3, \quad (17)$$

with  $H(T)$  the Hubble constant determined by the first Friedmann equation and  $v_w$  the bubble wall expansion velocity. When  $F(T)$  drops to 0.71, the true vacuum bubbles are able to form an infinite connected cluster, denoted as percolation [73], and the corresponding temperature  $T_*$  is adopted as the FOPT temperature. For a small  $g_X$ , the action scales as  $S_3/T \propto g_X^{-3}$  [42], resulting in a highly suppressed tunneling rate and hence a supercooled transition with  $T_* \ll w$ . In extreme cases, if percolation cannot occur before  $T_{\text{QCD}} \approx 85$  MeV, the QCD phase transition will dramatically alter the structure of Eq. (15). The resulting cosmological histories fall into two main patterns, comprising four distinct types classified in Ref. [50].

If  $F(T)$  reaches 0.71 at  $T_* > T_{\text{QCD}}$ , the evolution follows the **normal pattern**. The high-scale  $SU(2)_X$  and conformal FOPT occurs first at  $T_*$ , and then affects the EW phase transition. This pattern can be further classified depending on the relation between  $T_*$  and the EW characteristic temperature  $T_{\text{ew}} \equiv m_h/\sqrt{2c_h} \approx 140$  GeV: **Type-N1** ( $T_* > T_{\text{ew}}$ ),  $SU(2)_X$  breaks via a FOPT at  $T_*$ , while the EW symmetry breaks via a smooth crossover near  $T_{\text{ew}}$ ; **Type-N2** ( $T_* < T_{\text{ew}}$ ), a joint  $SU(2)_X$ -EW FOPT takes place at  $T_*$ .

If  $\Gamma(T)$  is sufficiently suppressed such that  $F(T) > 0.71$  persists down to  $T_{\text{QCD}}$ , the evolution enters the **inverted pattern**. The Universe stays in the symmetric phase  $(0, 0)$  down to  $T_{\text{QCD}}$ , and a first-order QCD confinement transition is triggered by six-flavor massless quarks [74–76]. This induces a Higgs VEV  $h = v_{\text{QCD}} \approx 100$  MeV via the top-quark condensate [38, 42], reshaping the potential along the  $s$ -direction via

$$\delta V_{\text{QCD}}(s, T) = \frac{\lambda_{hs}}{4} h^2 s^2 \Big|_{h \rightarrow v_{\text{QCD}}} \approx -\frac{m_h^2 v_{\text{QCD}}^2}{4w^2} s^2, \quad (18)$$

adding to the thermal potential  $V_T(s, T)$  in Eq. (15). This negative mass-squared term for  $s$  lowers or even dismisses the barrier form by the  $T^2 s^2$  term, thereby qualitatively altering the tunneling behavior. The subsequent dynamics is determined by the ordering between  $T_{\text{QCD}}$  and the rolling temperature  $T_{\text{roll}} \equiv m_h v_{\text{QCD}} / (g_X w \sqrt{1 - g_X/\pi})$  that the barrier disappears: **Type-I1** ( $T_{\text{QCD}} > T_{\text{roll}}$ ), after the QCD FOPT, an  $SU(2)_X$  FOPT occurs at  $T_* \approx T_{\text{roll}}$ , which then drives the Higgs field from  $v_{\text{QCD}}$  to its final VEV  $v$ ; **Type-I2** ( $T_{\text{QCD}} < T_{\text{roll}}$ ), the QCD FOPT instantaneously triggers a joint  $SU(2)_X$ -EW FOPT at  $T_* = T_{\text{QCD}}$ , and a modeling of QCD phase transition dynamics is necessary [49].

### B. Transition regimes in the $(m_X, m_s)$ plane

Using the complete one-loop thermal potential listed in Appendix B, we calculate the FOPT dynamics within the CC  $SU(2)_X$  model and classify each point in the  $(m_X, m_s)$  parameter space according to its cosmological evolution type. All four types of evolution history involve an  $SU(2)_X$  FOPT. We characterize this transition by two standard parameters: the ratio of latent heat to the radiation energy density

$$\alpha = \frac{1}{\pi^2 g_* T_*^4 / 30} \left( \Delta V_T - \frac{T}{4} \frac{d\Delta V_T}{dT} \right) \Big|_{T_*}, \quad (19)$$

where  $\Delta V_T$  is the positive potential-energy difference between the true and false vacua and  $g_*$  is the number of effective degrees of freedom (d.o.f.) for energy; and the Hubble time relative to the duration of the transition,

$$\frac{\beta}{H} = T \frac{d(S_3/T)}{dT} \Big|_{T_*}. \quad (20)$$

<sup>1</sup> Lattice simulations show that the transition still proceeds as a FOPT even when  $T$  is very close to  $T_{\text{roll}}$  and the barrier is sufficiently low [77].

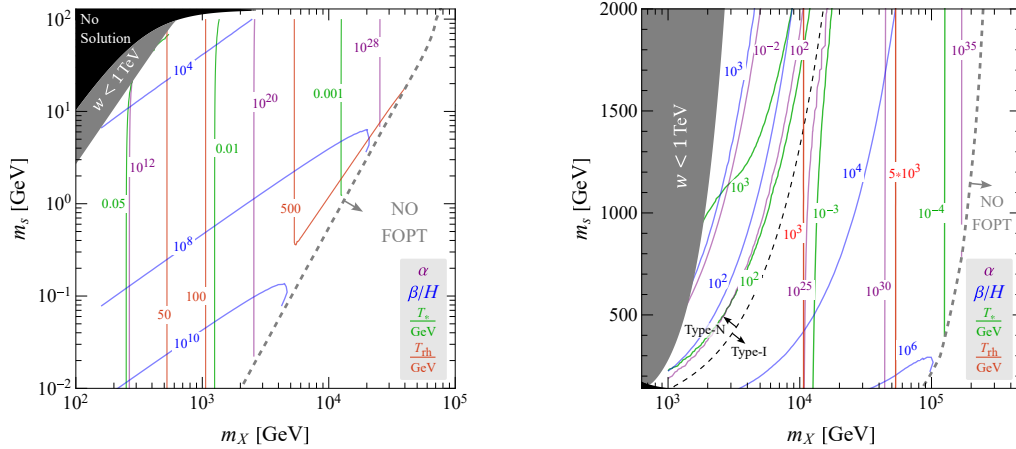


FIG. 1. Contours of FOPT characteristic parameters  $\alpha$  (purple),  $\beta/H$  (blue),  $T_*$  (green), and  $T_{\text{th}}$  (red) for  $m_s < m_h$  (left) and  $m_s > m_h$  (right). The black and gray shaded areas denote the unphysical and  $w < 1$  TeV regions, respectively, while the gray dashed line separates FOPT from non-FOPT areas. In the right panel, the black dashed line is the boundary of different thermal history patterns.

It is convenient to express the vacuum energy density in terms of a characteristic temperature scale,  $T_\Lambda$ , defined by  $\pi^2 g_* T_\Lambda^4 / 30 = \Delta V_T$ . The release of vacuum energy during the FOPT reheats the Universe from  $T_*$  to  $T_{\text{rh}}$  [19],

$$T_{\text{rh}} = T_\Lambda \times \min \left( 1, \frac{\Gamma_{\text{eff}}}{H(T_*)} \right)^{1/2}, \quad (21)$$

where  $\Gamma_{\text{eff}} = \Gamma_h \sin^2 \theta + \Gamma_s \cos^2 \theta$  with  $\Gamma_h$  and  $\Gamma_s$  being the decay width of the  $h$  and  $s$  bosons, respectively. In the supercooled regime ( $\alpha \gg 1$ ),  $T_\Lambda \approx (1 + \alpha)^{1/4} T_*$ .

The FOPT characteristic parameters are displayed in Fig. 1, where the left and right panels correspond to  $m_s < m_h$  and  $m_s > m_h$ , respectively. The gray shaded regions represent  $w < 1$  TeV, where the sequential symmetry breaking assumption is invalid, while the black regions do not satisfy Eq. (8) and hence have no physical solution to  $w$ .

In the left panel, only the Type-II evolution is observed. This scenario is characterized by extremely supercooled FOPT with ultrashort duration. Specifically, the parameters typically fall within the ranges of  $T_* = \mathcal{O}(1 - 100)$  MeV,  $T_{\text{th}} = \mathcal{O}(10^2)$  GeV, and  $\beta/H = \mathcal{O}(10^4 - 10^{10})$ . Notably, the contour lines for  $\alpha$  and  $T_*$  are almost parallel to the  $m_s$  axis. This behavior arises because both the potential difference  $\Delta V_T$  and the FOPT temperature  $T_*$  ( $\approx T_{\text{roll}}$  in Type-II) are dominated by  $m_X = g_X w$ , while being largely insensitive to  $m_s$ . Regarding  $T_{\text{th}}$ , in the limit of instantaneous reheating, the temperature scales as  $m_X$ . This trend arises from the significant sensitivity to  $\alpha$  (or equivalently  $\Delta V_T$ ). The kink appearing at the  $T_{\text{th}} = 500$  GeV contour signifies the transition into the region of slow reheating, i.e.,  $\Gamma_{\text{eff}} < H(T_*)$ . The contours of  $\beta/H$  run nearly parallel to those of the coupling  $g_X$ , e.g.,  $\beta/H = 10^4$  ( $10^8$ ) roughly overlaps with  $g_X = 10^{-1}$  ( $10^{-3}$ ), except some kinks near the gray dashed line. A detailed explanation of this alignment is provided in Appendix C.

As for the right panel of Fig. 1, both Type-N and Type-

II evolution paths are possible, divided by the black dashed line. In the Type-N region, FOPT occurs at relatively high temperatures,  $T_* = \mathcal{O}(10^2 - 10^3)$  GeV, accompanied by mild supercooling. Conversely, to the right of the black dashed line, we recover the Type-II pattern with extremely supercooled FOPT. Here,  $T_*$  drops significantly to  $\mathcal{O}(0.1 - 100)$  MeV, while  $\beta/H$  reaches  $\mathcal{O}(10^4 - 10^6)$ . Within this domain,  $\alpha$  and  $T_*$  are primarily determined by  $m_X$ , and hence their contours remain nearly parallel to the  $m_s$  axis.

In both panels, regions without a FOPT appear to the right of the gray dashed lines. In these regions, percolation never exists as the temperature drops to  $T_{\text{roll}}$ , indicating that the transition is instead second-order or crossover. Technically, this behavior stems from two effects in the small- $g_X$  limit. First, as  $T \rightarrow T_{\text{roll}}$ , the action  $S_3/T \sim g_X^{-3} (1 - T_{\text{roll}}/T)^{3/2}$ , which makes  $\Gamma(T) \rightarrow 0$  due to the prefactor in Eq. (16). We have checked that even in this limit the contribution from  $O(4)$ -symmetric action is still negligible. Second, the transition duration becomes extremely short, with  $\beta/H \propto g_X^{-2}$ , leaving insufficient time for bubbles to nucleate and percolate. However, one should note that this conclusion relies on the one-loop effective potential and the semiclassical tunneling rate. The situation may differ if a rigorous calculation involving higher-order corrections to the effective potential [78–80] and the functional determinant of the tunneling rate [81–83] is performed.

#### IV. THREE DARK MATTER SCENARIOS

Based on the thermal history outlined above, three DM scenarios arise in the CC  $SU(2)_X$  model. The charged  $X^\pm$  bosons can constitute particle DM, realized either via WIMP freeze-out or as supercooled DM, depending on their thermalization following the FOPT. In addition, the triplet  $SU(2)_X$  model has a monopole DM candidate. We examine

each scenario in turn.

### A. Particle dark matter: WIMP or supercooling

Before the  $SU(2)_X$  FOPT, the gauge bosons  $X^\pm$  and  $A'$  are massless, with an abundant number density  $\sim T^3$  in the thermal bath. The equilibrium yield of  $X^\pm$  in the symmetric phase can be obtained from the massless Bose-Einstein distribution, i.e.,

$$Y_{\text{eq}}^s \equiv \frac{3\zeta_3 T^3 / \pi^2}{2\pi^2 g_{*s} T^3 / 45} = \frac{135\zeta_3}{2\pi^4 g_{*s}}, \quad (22)$$

where  $\zeta_3 \approx 1.202$ ,  $g_{*s}$  is the number of effective d.o.f. for entropy. Note that only one sign of  $X^\pm$  ( $X^+$  or  $X^-$ ) is counted in Eq. (22). The FOPT drastically alters this picture through two effects: mass gain and entropy injection.

During the  $SU(2)_X$  FOPT, the charged bosons  $X^\pm$  acquire a mass  $m_X^* = g_X w_*$  inside the bubble, where  $w_*$  is the true vacuum value of  $s$  at  $T_*$ . In a moderate FOPT, if  $m_X^* \gg T_*$ , most  $X^\pm$  bosons lack sufficient kinetic energy to penetrate the bubble wall due to the repulsive force induced by the mass gap [84–86]. However, in a supercooled FOPT, the wall velocity  $v_w \approx 1$ , yielding a huge Lorentz factor  $\gamma_w = (1 - v_w^2)^{-1/2} \gg 1$ . In the wall frame, the incident particles are boosted to energies  $\sim \gamma_w T_* \gg m_X^*$ , enabling all of them to enter the bubble [65–67]. Despite complete penetration, the final abundance of  $X^\pm$  is diluted by the entropy release during the post-FOPT reheating. The resulting abundance of  $X^+$  or  $X^-$  particles right after reheating is [19]

$$Y_{\text{rh}} = Y_{\text{eq}}^s \left( \frac{T_{\text{rh}}}{T_\Lambda} \right) \left( \frac{T_*}{T_\Lambda} \right)^3, \quad (23)$$

which serves as the initial condition for subsequent DM evolution. For the supercooled transition we consider,  $Y_{\text{rh}}$  is typically highly suppressed and negligible, and  $w_* \approx w$  is a rather accurate approximation.

Following the FOPT, the scalar fields undergo coherent oscillations around the vacuum and decay into SM light particles, such as  $e^+e^-$ ,  $\nu\bar{\nu}$ , or  $b\bar{b}$ , generating a thermal plasma, and the Universe then enters a radiation era. In the parameter space of interest,  $s$  can thermalize via the interactions with the SM particles. The  $X^\pm$  bosons can then be produced through annihilations of  $s$  or SM particles. For a prompt reheating,  $\Gamma_{\text{eff}} > H_*$ , the evolution of  $X^\pm$  is then described by the Boltzmann equation

$$\frac{dY}{dz} = \sqrt{\frac{\pi g_{*s}^2}{45 g_*}} \frac{M_{\text{Pl}} m_X}{z^2} \langle \sigma v_{\text{rel}} \rangle [(Y_{\text{eq}}^b)^2 - Y^2], \quad (24)$$

where  $M_{\text{Pl}} = 1.22 \times 10^{19}$  GeV is the Planck scale,  $Y$  denotes the  $X^+$  or  $X^-$  yield (i.e., number density over the entropy density) after the FOPT,

$$Y_{\text{eq}}^b \equiv \frac{3m_X^2 T K_2(m_X/T) / (2\pi^2)}{2\pi^2 g_{*s} T^3 / 45} = \frac{135z^2 K_2(z)}{4\pi^4 g_{*s}} \quad (25)$$

is the equilibrium yield in the  $SU(2)_X$ -breaking phase with  $K_2(z)$  the modified Bessel function of the second kind,  $z \equiv m_X/T$ , and  $\langle \sigma v_{\text{rel}} \rangle$  is the thermally averaged annihilation cross section whose details are given in Appendix D. The dominant annihilation channels contributing to  $\langle \sigma v_{\text{rel}} \rangle$  are

$$X^+ X^- \rightarrow ss; \quad X^+ X^- \rightarrow W^+ W^- / ZZ / t\bar{t}, \quad (26)$$

where annihilations into SM final states proceed via off-shell  $h$  or  $s$  bosons.

The evolution described by Eq. (24) begins at  $z_{\text{rh}} \equiv m_X/T_{\text{rh}}$  with the initial condition  $Y(z_{\text{rh}}) = Y_{\text{rh}}$ . The resulting relic abundance is determined by the relationship between the  $X^\pm$  annihilation rate

$$\Gamma_{\text{ann}} \equiv \left( \frac{2\pi^2}{45} g_{*s} T_{\text{rh}}^3 \right) Y_{\text{eq}}^b \langle \sigma v_{\text{rel}} \rangle \Big|_{T_{\text{rh}}} \quad (27)$$

and the Hubble parameter  $H_{\text{rh}} \equiv H(T_{\text{rh}})$  at the reheating temperature. If  $\Gamma_{\text{ann}} > H_{\text{rh}}$ , the  $X^\pm$  bosons rapidly thermalize and subsequently undergo conventional thermal freeze-out. This yields the familiar WIMP miracle [87]

$$\Omega_{\text{fo}} h^2 \approx 2 \times \frac{2.55 \times 10^{-10} \text{ GeV}^{-2}}{\langle \sigma v_{\text{rel}} \rangle}. \quad (28)$$

Conversely, if  $\Gamma_{\text{ann}} < H_{\text{rh}}$ , the  $X^\pm$  bosons never reach thermal equilibrium. Their abundance is instead set by a freeze-in mechanism, with the asymptotic yield given by [54]

$$Y_\infty \approx Y_{\text{rh}} + \frac{135\sqrt{5} M_{\text{Pl}} m_X \langle \sigma v_{\text{rel}} \rangle}{128\pi^{13/2} g_{*s} \sqrt{g_*}} (1 + 2z_{\text{rh}}) e^{-2z_{\text{rh}}}, \quad (29)$$

and the corresponding relic density is

$$\Omega_{\text{sc}} h^2 = 2Y_\infty s_0 m_X \frac{8\pi}{3M_{\text{Pl}}^2} \left( \frac{h}{H_0} \right)^2, \quad (30)$$

where  $s_0 \approx 2891 \text{ cm}^{-3}$  is the present entropy density [88] and  $H_0/h = 100 \text{ km}/(\text{s} \cdot \text{Mpc})$ . This production mechanism is referred to as supercooled DM [19, 20, 54, 55].<sup>2</sup> In this scenario, typically  $z_{\text{rh}} \gtrsim 20$ , and the expression simplifies to the useful approximate form

$$\Omega_{\text{sc}} h^2 \approx \left( \frac{m_X}{\text{TeV}} \right)^2 \left( \frac{z_{\text{rh}}}{23} \right) \frac{e^{-2(z_{\text{rh}}-23)} \langle \sigma v_{\text{rel}} \rangle}{2.43 \times 10^{-10} \text{ GeV}^{-2}}. \quad (31)$$

This highlights the key features that distinguish supercooled DM from WIMP freeze-out: the relic density is proportional to  $\langle \sigma v_{\text{rel}} \rangle$ , and it exhibits an exponential Boltzmann suppression from  $m_X/T_{\text{rh}}$ . It should be noted that Eqs. (28) and (31) are provided for illustration; in our analysis, the relic abundance is obtained by numerically solving the full Boltzmann equation in Eq. (24).

<sup>2</sup> Similar mechanism for a low inflationary reheating temperature is also possible [89, 90].

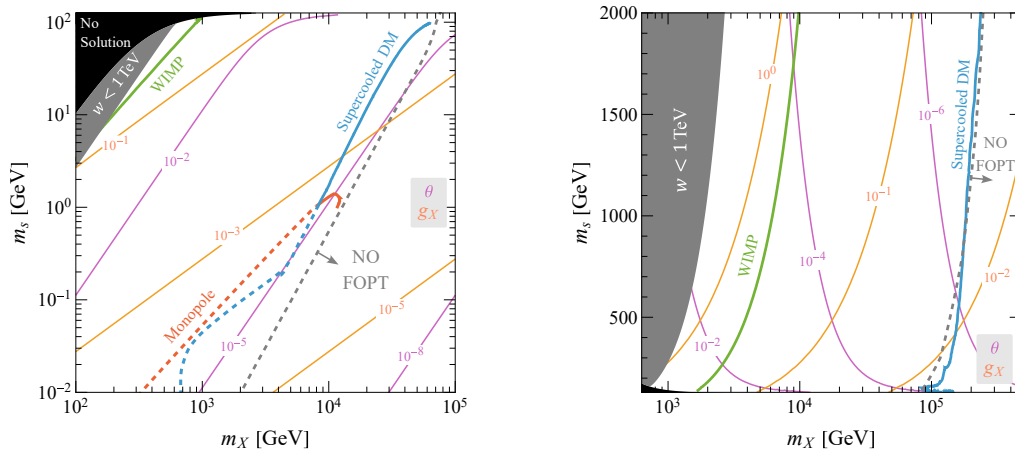


FIG. 2. Valid DM scenarios in the  $(m_X, m_s)$  plane for  $m_s < m_h$  (left) and  $m_s > m_h$  (right). Bold colored curves indicate parameter space with the correct DM relic abundance: WIMP (green), supercooled DM (blue), and monopole DM (red, left panel only). Contours of  $g_X$  and  $\theta$  are shown as orange and magenta contours, respectively. All other conventions follow Fig. 1.

We comment on the possible presence of a dark radiation background today. After the FOPT, the yield of  $A'$  is diluted to be negligible by the entropy production, and  $A'$  cannot re-thermalize. This is because the plasma after reheating only contains SM particles and the  $s$  bosons: the SM particles do not directly couple to  $A'$ , while the loop-induced  $sA'A'$  coupling is suppressed by the large  $SU(2)_X$  breaking scale and not sufficient to thermalize  $A'$ . Consequently, the evolution of  $A'$  is tied to that of the  $X^\pm$  bosons via the unsuppressed  $X^+X^-A'$  vertex. In the WIMP freeze-out scenario,  $X^\pm$  thermalizes and reproduces the dark photon bath via  $X^+X^- \rightarrow A'A'$ . By contrast, in the supercooled DM scenario,  $X^\pm$  never reaches equilibrium, and no significant dark photon bath is regenerated after the transition.

### B. Topological soliton dark matter: monopole

The triplet  $SU(2)_X$  model supports a topological soliton, known as the 't Hooft-Polyakov monopole [24, 25]. For  $m_X \gtrsim m_s$ , the monopole has a radius  $R_{\text{mp}} \approx m_X^{-1}$  and a mass  $M_{\text{mp}} \approx 4\pi w/g_X$  [91]. These monopoles are formed in the early Universe via the Kibble-Zurek mechanism when the  $SU(2)_X \rightarrow U(1)_X$  symmetry breaking occurs [92, 93]. In our CC model, this breaking is driven by a FOPT. Consequently, the number density of monopoles immediately after formation can be estimated from the density of true vacuum bubbles at  $T_*$ , parametrized as [94, 95]

$$n_{\text{mp}}^* = pn_b^*, \quad (32)$$

where  $p \sim 10^{-1}$ , and  $n_b^* = \beta^3/(8\pi v_w^3) \approx 0.04\beta^3/v_w^3$  is the bubble number density.

After production, monopoles and antimonopoles may undergo annihilation, whose evolution is generally described by a set of Boltzmann equations [96]. However, if no

dark-photon thermal bath exists following the FOPT, annihilation processes are strongly suppressed, and the monopoles simply free-stream without significant interaction [91]. In this case, their number density is solely diluted by the entropy production during reheating, and they scale as cold DM thereafter. The present-day relic abundance is then given by

$$\Omega_{\text{mp}} h^2 = \frac{n_{\text{mp}}^* T_{\text{rh}}}{s_* T_\Lambda} \left(\frac{T_*}{T_\Lambda}\right)^3 s_0 M_{\text{mp}} \frac{8\pi}{3M_{\text{Pl}}^2} \left(\frac{h}{H_0}\right)^2, \quad (33)$$

where  $s_* = 2\pi^2 g_* T_*^3/45$  is the entropy density at FOPT.

## V. PHENOMENOLOGY

Combining the cosmological history and DM mechanisms discussed in Sections III and IV, we now identify the viable DM parameter space of our model. We require each DM candidate to reproduce the observed relic abundance  $\Omega_{\text{DM}} h^2 \approx 0.12$ , and subsequently examine its multi-messenger signatures, ranging from terrestrial particle physics experiments, including DM direct detection, LHC searches, and long-lived particle (LLP) frontiers, to cosmological gravitational wave (GW) observatories.

### A. Landscape of dark matter scenarios

The DM parameter space in the  $(m_X, m_s)$  plane is shown in Fig. 2, where curves corresponding to the correct relic abundance are highlighted for three distinct scenarios: WIMP (green), supercooled DM (blue), and monopole DM (red, only in  $m_s < m_h$  region). In the WIMP regime, the post-FOPT reheating temperature satisfies  $z_{\text{rh}} \lesssim 20$ , such that the  $X^\pm$  bosons efficiently thermalize with the plasma. Their final abundance is then determined by the standard freeze-out

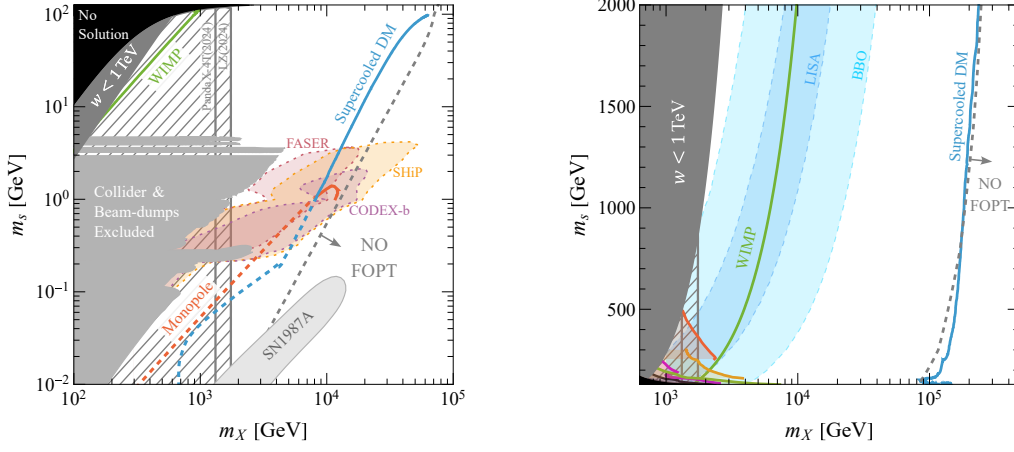


FIG. 3. Experimental constraints and projected sensitivities in the  $(m_X, m_s)$  plane for  $m_s < m_h$  (left) and  $m_s > m_h$  (right). Medium gray: collider and beam-dump experiment exclusions; light gray: astrophysical bound from SN1987A; hatched gray: direct detection limits. Colored dashed contours (left) show the projected reach of LLP searches. Blue and light-blue shaded regions (right) indicate the sensitivity of LISA and BBO to the stochastic GW background from the FOPT. Colored regions near  $m_X \sim \text{TeV}$  (right) depict collider constraints and projections (see Fig. 4 for details). Other conventions follow Figs. 1 and 2.

condition, leading to the familiar inverse dependence on the annihilation cross section. This region is typically associated with EW-size gauge couplings,  $g_X \sim 10^{-1}$ , and a DM mass  $m_X$  around the TeV scale.

The supercooled DM scenario differs significantly from the WIMP case. The smaller gauge couplings prevent the  $X^\pm$  bosons from reentering thermal equilibrium, leading to a freeze-in production mechanism. While the small couplings drive a significant deviation from the typical  $z_{\text{rh}} \sim 20$ , the model characteristically yields  $z_{\text{rh}} \sim 10$  within the instant reheating regime; the high reheating temperature  $T_{\text{rh}}$  generated by the supercooling allows for a heavier DM mass spectrum, occupying a distinct region with  $m_X = \mathcal{O}(10 - 10^2)$  TeV and significantly reduced couplings  $g_X = \mathcal{O}(10^{-2} - 10^{-3})$ . The parameter space between the WIMP and supercooled DM lines marks a region in which the  $X^\pm$  bosons are overproduced.

In the left panel of Fig. 2 where  $m_s < m_h$ , the 't Hooft-Polyakov monopoles provide a DM candidate when the FOPT is extremely rapid. Their abundance follows the Kibble-Zurek mechanism: a larger  $\beta/H$  indicates a faster transition and a higher density of nucleated bubbles, thereby enhancing monopole production. The observed relic density is achieved along the red line, corresponding to  $\beta/H \sim 10^9$ , and the corresponding monopole mass is  $M_{\text{mp}} \sim 10^{12}$  GeV. To the lower-right, larger  $\beta/H$  yields monopole overproduction. The intersection of the monopole and supercooled DM lines creates mutually exclusive regions; the zones where their combined abundance exceeds the observed limit are indicated by dashed lines. It should be noted, however, that the monopole abundance from Eq. (32) is a rough approximation, and the precise location of the red line is subject to refinement through detailed simulations.

Our result stands in contrast to Ref. [97], which argues that the  $X^\pm$  abundance always dominates over the monopoles,

precluding monopoles as a viable DM candidate. The difference arises from the CC feature of our model, which yields a logarithmic potential rather than the polynomial form in Ref. [97], enabling an extremely supercooled FOPT with large enough  $\beta/H$ .

## B. Experimental constraints and projections

The phenomenological viability is summarized in Fig. 3. In the left panel where  $m_s < m_h$ , terrestrial experiments, including LHCb [98, 99], NA62 [100, 101], CHARM [102], E949 [103], LSND [104], and MicroBooNE [105], constrain the mixing angle  $\theta$  between  $s$  and  $h$ , yielding the medium-gray exclusion region. Astrophysical bounds from SN1987A, based on energy-loss arguments [102], further restrict the parameter space. In addition, the  $X^\pm$  bosons interact with each other via a long-range force mediated by the massless  $A'$ , potentially leaving imprints on astronomical observables such as the ellipticity of the gravitational potential of NGC720 [106–108]. In our model, however, this constraint is subdominant, and is therefore omitted from the figure.

Another constraint arises from the DM direct detection, which sets bound on the spin-independent (SI) scattering cross section between  $X^\pm$  and a nucleon  $N$ . This observable can be systematically analyzed within an effective field theory framework (see, e.g., Ref. [109]). In our model, the interaction is controlled by the renormalizable Higgs portal coupling, yielding [110]

$$\sigma_{\text{SI}} = \frac{\mu_{XN}^2 g_X^4 \sin^2 2\theta}{\pi 4v^2} m_N^2 f_N^2 \left( \frac{1}{m_h^2} - \frac{1}{m_s^2} \right)^2 \quad (34)$$

where  $\mu_{XN} = m_X m_N / (m_X + m_N)$  is the reduced mass of the DM-nucleon system, and  $f_N \approx 0.3$  [111] is the effective

nucleon coupling. As  $\theta$  decreases with increasing  $w$ , this cross section is naturally suppressed for heavier DM. Comparing our parameter space with the latest limits from LZ [112] and PandaX-4T [113] yields the hatched gray exclusion region shown in the figure, where the entire WIMP scenario is now ruled out.

The supercooled DM and monopole DM scenarios remain viable under current experimental constraints. Their indirect detection, however, is possible through LLP searches targeting the neutral scalar  $s$ . As shown in the left panel of Fig. 3, both non-WIMP scenarios occupy the large- $w$  region, where the mixing angle  $\theta$  between  $s$  and  $h$  is highly suppressed. This suppression leads to a correspondingly small total decay width  $\Gamma_s \propto \sin^2 \theta$ , rendering  $s$  sufficiently long-lived to be accessible at future LLP searches. The colored dashed contours in Fig. 3 indicate the projected sensitivities of experiments such as FASER [114], CODEX-b [115], and SHiP [116].

In the right panel of Fig. 3 ( $m_s > m_h$ ), both the WIMP and supercooled DM scenarios are allowed by current experimental limits, although WIMP masses below  $\sim 2$  TeV are excluded by direct detection. The WIMP region can be efficiently probed via GWs from the FOPT. Detectable signals fall within the sensitivity reach of future space-based interferometers such as LISA [117] and BBO [118], as delineated by the blue and light-blue regions. Detectability is defined by a signal-to-noise ratio exceeding 50, evaluated using standard numerical formulas [119, 120] for an integration time of  $\mathcal{T} = 0.75 \times 4$  years. TianQin [121] and Taiji [122] are expected to achieve comparable sensitivity. In contrast, as emphasized in Ref. [50], the  $m_s < m_h$  regime has an extremely strong yet short-lived FOPT, making its GW signal undetectable.

Another indirect probe for the WIMP scenario in the  $m_s > m_h$  regime is the prompt decay of  $s$ , as shown in the right panel of Fig. 3 (see Fig. 4 for a detailed view). Current bounds are displayed as black contours, which combine LHC Run 2 constraints from Higgs signal strength measurements [6] ( $36.1 - 139 \text{ fb}^{-1}$ ) and BSM  $s \rightarrow ZZ$  searches [123] ( $35.9 \text{ fb}^{-1}$ ). Extrapolating these to the HL-LHC ( $3000 \text{ fb}^{-1}$ ) yields the purple contour, which offers significant coverage for  $m_h \lesssim m_s \lesssim 2m_h$ , with a notable dip near  $m_s \sim 170$  GeV due to branching ratio suppression [124]. Probing deeper into the parameter space requires a future 10 TeV muon collider ( $\mu\text{C}$ ), where vector boson fusion (VBF) production of  $s$  can reach sensitivities down to  $\theta \sim 10^{-2}$ . The reach varies across decay channels, reflecting the dominant branching fractions of  $s$ :  $s \rightarrow b\bar{b}$  (light green) and  $s \rightarrow VV$  (orange) offer significantly broader coverage than  $s \rightarrow hh$  (red). For a detailed phenomenological analysis of these VBF processes at the  $\mu\text{C}$ , see Ref. [50].

## VI. CONCLUSION

This work investigates three DM scenarios and their phenomenology within the CC  $SU(2)_X$  gauge theory, where the dark scalar resides in the triplet representation. EW symmetry breaking is triggered dynamically by the  $SU(2)_X$  sector via

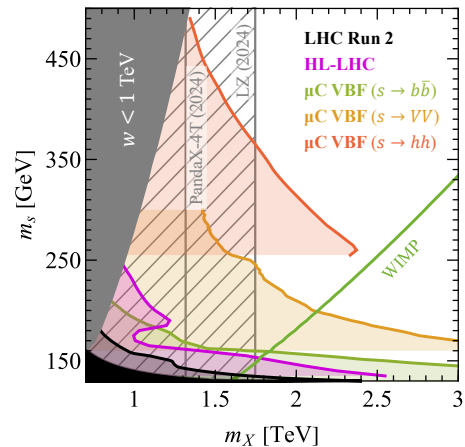


FIG. 4. Zoomed-in view of the right panel of Fig. 3. Shaded regions show collider constraints and projections: LHC Run 2 (semi-transparent black), HL-LHC extrapolation (purple), and a 10 TeV muon collider ( $\mu\text{C}$ ) with  $s$  produced via VBF and decaying to  $b\bar{b}$  (light green),  $VV$  (orange), and  $hh$  (red). Conventions follow Fig. 3.

the CW mechanism, thereby relaxing the hierarchy problem. Beyond the conventional WIMP, the model accommodates two additional DM candidates: supercooled DM, arising from the unique FOPT process in the CC theory, and topological monopole, enabled by the adjoint representation of the scalar field.

The minimality of the CC theory allows the entire parameter space to be concisely represented in the two-dimensional plane  $(m_X, m_s)$ , offering a unified perspective on the DM phenomenology. In the light scalar regime ( $m_s < m_h$ ), all three DM scenarios emerge. Notably, contrary to earlier claims, monopole DM remains a viable candidate. While the WIMP region is already excluded by direct detection experiments, the supercooled and monopole DM scenarios survive, and can be probed via future LLP searches. In the heavy scalar regime ( $m_s > m_h$ ), only the WIMP and supercooled DM scenarios persist. The WIMP candidate can be explored through a combination of collider and GW experiments, whereas the supercooled DM lies beyond the reach of current and foreseeable experiments.

This work can be further extended in several directions. First, more direct probes of supercooled and monopole DM (beyond indirect sensitivity via the scalar  $s$ ) remain to be explored. Second, based on the standard one-loop effective potential and semiclassical vacuum decay rate, our analysis reveals a region at large  $m_X$  where the FOPT does not occur. A definitive assessment of this regime calls for higher-order corrections and a more refined treatment of the vacuum tunneling rate. Third, since the post-FOPT reheating inevitably dilutes any preexisting relics, including the baryon asymmetry, an appropriate baryogenesis mechanism must be incorporated.

## ACKNOWLEDGMENTS

We thank Shao-Ping Li for the helpful discussions and comments. This work is supported by the National Science Foundation of China under Grant No. 12305108.

### Appendix A: Parametrization scheme

Define  $B = 3g_X^4/(4\pi^2)$ , following Ref. [50], the model parameters can be re-parametrized as

$$\begin{aligned} \lambda_{hs} &= \frac{w(m_s^2 + m_h^2) \pm \mathcal{C}}{-2w(v^2 + w^2)}, \\ B &= \frac{(m_s^2 + m_h^2)w \mp \mathcal{C}}{2w^3}, \\ \tan \theta &= \frac{\pm 2m_h^2 v}{\pm(m_h^2 - m_s^2)w + \mathcal{C}}, \end{aligned} \quad (\text{A1})$$

for  $m_s \leq m_h$ , and  $\lambda_h = -\lambda_{hs}w^2/(2v^2)$ , where  $\mathcal{C} = \sqrt{w^2(m_h^2 - m_s^2)^2 - 4m_s^2m_h^2v^2}$ .

Since  $w \gg v$ , we can expand the fields around the vacuum to obtain the interactions between physical particles, i.e.,

$$\begin{aligned} \mathcal{L}_3 &= -\frac{m_h^2}{2v}h^3 + \frac{m_h^2(2m_h^2 + m_s^2)}{2w(m_s^2 - m_h^2)}h^2s \\ &\quad + \frac{m_h^2m_s^2v(m_h^2 - 4m_s^2)}{2w^2(m_h^2 - m_s^2)^2}hs^2 - \frac{5m_s^2}{6w}s^3, \end{aligned} \quad (\text{A2})$$

for triple couplings, and

$$\mathcal{L}_4 = -\frac{m_h^2}{8v^2}h^4 + \mathcal{L}_{h^3s} + \mathcal{L}_{h^2s^2} + \mathcal{L}_{hs^3} - \frac{11m_s^2}{24w^2}s^4, \quad (\text{A3})$$

with

$$\begin{aligned} \mathcal{L}_{h^3s} &= -\frac{m_h^4}{2} \left[ \frac{(m_s^4 - 2m_h^4)v}{(m_h^2 - m_s^2)^3 w^3} + \frac{1}{(m_h^2 - m_s^2)vw} \right] h^3s, \\ \mathcal{L}_{h^2s^2} &= \frac{m_h^2}{4w^2} \left[ 1 - \frac{3m_h^4}{(m_s^2 - m_h^2)^2} \right] h^2s^2, \\ \mathcal{L}_{hs^3} &= \frac{m_h^2(5m_h^4m_s^2 - 19m_h^2m_s^4 + 11m_s^6)v}{6(m_h^2 - m_s^2)^3 w^3} hs^3, \end{aligned} \quad (\text{A4})$$

for quartic couplings, regardless of the mass ordering between  $h$  and  $s$ .

### Appendix B: Complete expression of the thermal potential

The complete form of the finite-temperature effective potential in Eq. (13) is detailed below. The thermal contribution from the dark sector,

$$\begin{aligned} V_X^T(s, T) &= \frac{3T^4}{\pi^2} J_B \left( \frac{g_X^2 s^2}{T^2} \right) \\ &\quad - \frac{g_X^3}{6\pi} T \left[ (s^2 + T^2)^{3/2} - s^3 \right], \end{aligned} \quad (\text{B1})$$

includes the one-loop thermal integral together with the daisy-resummation correction for the longitudinal modes of the  $SU(2)_X$  gauge bosons. For the SM sector, the thermal potential is

$$V_h^T(h, T) = \sum \frac{n_i T^4}{2\pi^2} J_{B/F} \left( \frac{M_i^2(h)}{T^2} \right) + V_{\text{SM}}^{\text{ds}}(h, T), \quad (\text{B2})$$

where the sum runs over SM d.o.f. Dominant contributions come from the EW gauge bosons, the top quark, and the scalars:

$$\begin{cases} M_W^2(h) = g^2 h^2/4, & n_W = 2 \times 3 = 6; \\ M_Z^2(h) = (g^2 + g'^2)h^2/4, & n_Z = 3; \\ M_t^2(h) = y_t^2 h^2/2, & n_t = N_c \times 4 = 12; \\ M_h^2(h) = 3\lambda_h h^2, & n_h = 1; \\ M_G^2(h) = \lambda_G h^2, & n_G = 3, \end{cases} \quad (\text{B3})$$

where  $g$  and  $g'$  are the gauge couplings of the  $SU(2)_L$  and  $U(1)_Y$  group, respectively. The daisy resummation term  $V_{\text{SM}}^{\text{ds}}(h, T)$  can be found from Ref. [125]. Here, the thermal integrals are

$$J_{B/F}(y) = \pm \int_0^\infty dx x^2 \log \left( 1 \mp e^{-\sqrt{x^2+y}} \right), \quad (\text{B4})$$

where the upper (lower) sign corresponds to bosons (fermions).

### Appendix C: Analytical estimates of extremely supercooled phase transition dynamics in Type-I

The physical origin of the ‘‘NO FOPT’’ region in Fig. 1 and the scaling behavior of the FOPT parameters admit a simple analytical understanding. The Euclidean action is given by

$$\frac{S_3}{T} = \frac{1}{T} \int_0^\infty 4\pi r^2 dr \left[ \frac{1}{2} \left( \frac{ds_b}{dr} \right)^2 + V_T(s_b(r), T) \right], \quad (\text{C1})$$

where  $s_b(r)$  is the  $O(3)$ -symmetric bounce solution from the equation of motion

$$\frac{d^2 s_b}{dr^2} + \frac{2}{r} \frac{ds_b}{dr} = \frac{dV_T(s, T)}{ds} \Big|_{s=s_b}, \quad (\text{C2})$$

subject to the boundary conditions

$$\frac{ds_b}{dr} \Big|_{r=0} = 0, \quad \lim_{r \rightarrow \infty} s_b(r) = 0. \quad (\text{C3})$$

In the regime of extreme supercooling, the phase transition occurs at a temperature  $T_*$  very close to  $T_{\text{roll}}$ . In this limit, the bounce solution is primarily determined by the structure of the potential barrier rather than the depth of the true vacuum.

Let  $s_1$  denote the position of the local maximum of  $V_T(s, T)$  separating the false vacuum at  $s = 0$  from the true vacuum basin, and let  $V_1 \equiv V_T(s_1, T)$  be the corresponding

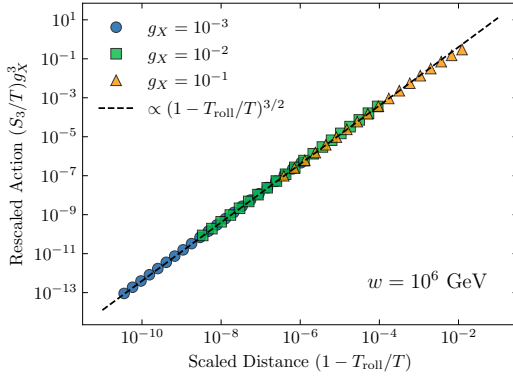


FIG. A1. Scaling of  $(S_3/T)g_X^3$  with  $(1 - T_{\text{roll}}/T)$ . At fixed  $w = 10^6$  GeV, numerical results for  $g_X = 10^{-1}$ ,  $10^{-2}$ , and  $10^{-3}$  collapse onto a universal line, confirming the analytical scaling of Eq. (C6) (dashed line).

barrier height. We further define  $s_0$  as the field value where the potential vanishes immediately after the barrier, i.e.,  $V_T(s_0, T) = 0$  for  $s_0 > s_1$ . To analyze the scaling behavior, we rescale the field, potential, and radial coordinate as follows:

$$\tilde{s} = \frac{s}{s_0}, \quad \tilde{V} = \frac{V_T(s, T)}{V_1}, \quad \tilde{r} = \sqrt{\frac{V_1}{s_0^2}} r. \quad (\text{C4})$$

In the CC  $SU(2)_X$  model,  $s_0 \sim T/g_X$  is determined by the competition between the thermal mass ( $\sim g_X T$ ) and the CW potential ( $\sim g_X^2$ ). Remarkably, the barrier height then scales as  $V_1 \sim T^4$ , independent of  $g_X$  up to an overall prefactor [42]. With the above rescaling, the thermal action factorizes as:

$$\frac{S_3}{T} = \frac{4\pi}{T} \frac{s_0^3}{\sqrt{V_1}} \tilde{S}_3 \equiv \frac{\mathcal{A}}{g_X^3} \tilde{S}_3(\tilde{T}), \quad (\text{C5})$$

where  $\mathcal{A}$  is a coefficient and  $\tilde{S}_3(\tilde{T})$  is a dimensionless shape

---


$$\langle \sigma_{ab \rightarrow cd} v_{\text{vel}} \rangle = \frac{(8m_a^2 m_b^2 T)^{-1}}{K_2(m_a/T) K_2(m_b/T)} \int d\hat{s} \sigma_{ab \rightarrow cd}(\hat{s}) \left[ 1 - \frac{(m_a + m_b)^2}{\hat{s}} \right] \left[ 1 - \frac{(m_a - m_b)^2}{\hat{s}} \right] \hat{s}^{3/2} K_1 \left( \frac{\sqrt{\hat{s}}}{T} \right), \quad (\text{D1})$$


---

where  $\sigma_{ab \rightarrow cd}(\hat{s})$  the initial-state-averaged cross section, and  $\hat{s}$  is the square of the center-of-mass energy. The dominant reaction channels for  $X^+ X^-$  annihilation in our study are listed in Eq. (26), i.e.,  $\langle \sigma v_{\text{vel}} \rangle \equiv \langle \sigma_{X^+ X^- \rightarrow ss} v_{\text{vel}} \rangle + \langle \sigma_{X^+ X^- \rightarrow \text{SM SM}} v_{\text{vel}} \rangle$ . Besides, we also consider the following processes

$$ss/sh \rightarrow hh/t\bar{t}/W^+ W^- / ZZ; \quad sZ \rightarrow W^+ W^-, \quad (\text{D2})$$

and all their crossed processes to verify that  $s$  can thermalize with the SM plasma after the FOPT.

Since the  $X^\pm$  bosons are charged under the residual

factor. Near  $T_{\text{roll}}$ , the shape factor could be evaluated by the thick-wall approximation, yielding [70]

$$\frac{S_3}{T} \propto \frac{1}{g_X^3} \left( 1 - \frac{T_{\text{roll}}}{T} \right)^{3/2}, \quad (\text{C6})$$

as illustrated in Fig. A1.

For extremely supercooled FOPT in the Type-I evolution pattern, the transition temperature  $T_* \approx T_{\text{roll}}$ , and the nucleation condition  $\Gamma(T_n)/H^4(T_n) = 1$  simplifies to

$$\frac{S_3}{T} \Big|_{T_n} \approx 4 \log \frac{M_{\text{Pl}} m_h v_{\text{QCD}}}{g_X^3 w^3}. \quad (\text{C7})$$

Over most of the parameter space,  $T_n$  closely tracks the percolation temperature  $T_*$ , allowing us to use the nucleation criterion to extract scaling behavior. Equating the bounce action in Eq. (C6) with Eq. (C7) reveals that  $(1 - T_{\text{roll}}/T_n) \sim g_X^2$  is required to compensate the prefactor  $g_X^{-3}$  in the action, yielding

$$\frac{\beta}{H} \sim \frac{1}{g_X^3} \frac{d}{dT} \left( 1 - \frac{T_{\text{roll}}}{T_n} \right)^{3/2} \sim g_X^{-2}, \quad (\text{C8})$$

which accounts for the alignment of  $g_X$  and  $\beta/H$  contours observed in Fig. 1. The kinks in the  $\beta/H$  contours near the “no FOPT” boundaries arise from the growing disparity between the nucleation and percolation conditions. In this region, the approximation  $T_n \approx T_*$  breaks down, rendering the above scaling analysis invalid.

#### Appendix D: Definition of $\langle \sigma v_{\text{rel}} \rangle$

For a Maxwell-Boltzmann distribution, the thermally averaged cross section for the process  $ab \rightarrow cd$  is [126]

---

$U(1)_X$ , they experience a long-range attractive force mediated by the massless dark photon  $A'$ . This interaction modifies the non-relativistic annihilation cross section through the Sommerfeld enhancement. To incorporate this effect, we multiply  $\langle \sigma v_{\text{vel}} \rangle$  by an extra factor  $\mathcal{S}$  [127]

$$\mathcal{S} = \frac{\pi \alpha_X / v_{\text{dm}}}{1 - e^{-\pi \alpha_X / v_{\text{dm}}}}, \quad (\text{D3})$$

with  $\alpha_X = g_X^2/(4\pi)$  and  $v_{\text{dm}} \approx \sqrt{6/z}$ . Although the Sommerfeld factor modestly increases the annihilation rate, it remains close to unity in the parameter region of interest due to the small values of  $g_X$ .

- [1] M. E. Peskin, Nucl. Phys. B **1018**, 116971 (2025), 2505.00694.
- [2] W. A. Bardeen, in *Ontake Summer Institute on Particle Physics* (1995).
- [3] K. A. Meissner and H. Nicolai, Phys. Lett. B **660**, 260 (2008), 0710.2840.
- [4] S. R. Coleman and E. J. Weinberg, Phys. Rev. D **7**, 1888 (1973).
- [5] R. Jackiw, Phys. Rev. D **9**, 1686 (1974).
- [6] G. Aad et al. (ATLAS), Phys. Rept. **1116**, 4 (2025), 2404.05498.
- [7] R. Hempfling, Phys. Lett. B **379**, 153 (1996), hep-ph/9604278.
- [8] S. Iso, N. Okada, and Y. Orikasa, Phys. Lett. B **676**, 81 (2009), 0902.4050.
- [9] S. Iso, N. Okada, and Y. Orikasa, Phys. Rev. D **80**, 115007 (2009), 0909.0128.
- [10] E. J. Chun, S. Jung, and H. M. Lee, Phys. Lett. B **725**, 158 (2013), [Erratum: Phys.Lett.B 730, 357–359 (2014)], 1304.5815.
- [11] A. Das, N. Okada, and N. Papapietro, Eur. Phys. J. C **77**, 122 (2017), 1509.01466.
- [12] S. Jung and K. Kawana, PTEP **2022**, 033B11 (2022), 2105.01217.
- [13] T. de Boer, M. Lindner, and A. Trautner, Phys. Lett. B **861**, 139241 (2025), 2407.15920.
- [14] N. Aghanim et al. (Planck), Astron. Astrophys. **641**, A6 (2020), [Erratum: Astron.Astrophys. 652, C4 (2021)], 1807.06209.
- [15] S. Yaser Ayazi and A. Mohamadnejad, JHEP **03**, 181 (2019), 1901.04168.
- [16] A. Mohamadnejad, Eur. Phys. J. C **80**, 197 (2020), 1907.08899.
- [17] V. Baules and N. Okada (2025), 2508.13527.
- [18] M. T. Frandsen, M. Heikinheimo, M. E. Thing, K. Tuominen, and M. Rosenlyst, Phys. Rev. D **108**, 015033 (2023), 2301.00041.
- [19] T. Hambye, A. Strumia, and D. Teresi, JHEP **08**, 188 (2018), 1805.01473.
- [20] I. Baldes and C. Garcia-Cely, JHEP **05**, 190 (2019), 1809.01198.
- [21] D. Borah, A. Dasgupta, and S. K. Kang, JCAP **12**, 039 (2021), 2109.11558.
- [22] M. Kierkla, A. Karam, and B. Swiezevska, JHEP **03**, 007 (2023), 2210.07075.
- [23] T. Hambye, JHEP **01**, 028 (2009), 0811.0172.
- [24] G. 't Hooft, Nucl. Phys. B **79**, 276 (1974).
- [25] A. M. Polyakov, JETP Lett. **20**, 194 (1974).
- [26] N. Baouche, A. Ahriche, G. Faisel, and S. Nasri, Phys. Rev. D **104**, 075022 (2021), 2105.14387.
- [27] N. Benincasa, L. Delle Rose, L. Panizzi, M. Razzaq, and S. Urzetta, Phys. Rev. D **112**, 095004 (2025), 2506.22248.
- [28] A. L. Foguel, R. Z. Funchal, and M. Frigerio (2025), 2510.26765.
- [29] S. Baek, P. Ko, and W.-I. Park, JCAP **10**, 067 (2014), 1311.1035.
- [30] V. V. Khoze and G. Ro, JHEP **10**, 061 (2014), 1406.2291.
- [31] I. Chaffey and P. Tanedo, Phys. Rev. D **101**, 075005 (2020), 1907.10217.
- [32] T. Ghosh, H.-K. Guo, T. Han, and H. Liu, JHEP **07**, 045 (2021), 2012.09758.
- [33] T. Nomura, H. Okada, and S. Yun, JHEP **06**, 122 (2021), 2012.11377.
- [34] Z. Hu, C. Cai, Y.-L. Tang, Z.-H. Yu, and H.-H. Zhang, JHEP **07**, 089 (2021), 2103.00220.
- [35] C.-H. Chen and T. Nomura, Phys. Lett. B **746**, 351 (2015), 1501.07413.
- [36] Z. Zhang, C. Cai, and H.-H. Zhang, Phys. Rev. D **106**, 115022 (2022), 2209.01980.
- [37] C.-X. Yuan, Z. Zhang, C. Cai, Y.-L. Tang, and H.-H. Zhang, Phys. Rev. D **111**, 015004 (2025), 2405.16165.
- [38] E. Witten, Nucl. Phys. B **177**, 477 (1981).
- [39] T. Konstandin and G. Servant, JCAP **12**, 009 (2011), 1104.4791.
- [40] R. Jinno and M. Takimoto, Phys. Rev. D **95**, 015020 (2017), 1604.05035.
- [41] C.-W. Chiang and E. Senaha, Phys. Lett. B **774**, 489 (2017), 1707.06765.
- [42] S. Iso, P. D. Serpico, and K. Shimada, Phys. Rev. Lett. **119**, 141301 (2017), 1704.04955.
- [43] C. Marzo, L. Marzola, and V. Vaskonen, Eur. Phys. J. C **79**, 601 (2019), 1811.11169.
- [44] L. Bian, W. Cheng, H.-K. Guo, and Y. Zhang, Chin. Phys. C **45**, 113104 (2021), 1907.13589.
- [45] J. Ellis, M. Lewicki, J. M. No, and V. Vaskonen, JCAP **06**, 024 (2019), 1903.09642.
- [46] J. Ellis, M. Lewicki, and V. Vaskonen, JCAP **11**, 020 (2020), 2007.15586.
- [47] K. Kawana, Phys. Rev. D **105**, 103515 (2022), 2201.00560.
- [48] A. Ahriche, S. Kanemura, and M. Tanaka, JHEP **01**, 201 (2024), 2308.12676.
- [49] L. Sagunski, P. Schicho, and D. Schmitt, Phys. Rev. D **107**, 123512 (2023), 2303.02450.
- [50] W. Liu and K.-P. Xie, Phys. Rev. D **110**, 115001 (2024), 2408.03649.
- [51] A. Salvio (2026), 2602.20246.
- [52] Z. Kang and J. Zhu, Phys. Rev. D **102**, 053011 (2020), 2003.02465.
- [53] V. V. Khoze and D. L. Milne, Phys. Rev. D **107**, 095012 (2023), 2212.04784.
- [54] X.-R. Wong and K.-P. Xie, Phys. Rev. D **108**, 055035 (2023), 2304.00908.
- [55] S. Y. Ayazi and M. Hosseini, Nucl. Phys. B **1020**, 117138 (2025), 2502.14526.
- [56] P. Athron, S. Datta, and Z.-Y. Zhang (2025), 2511.10288.
- [57] D. Racco and A. Stanzione (2025), 2512.16809.
- [58] I. Baldes and M. O. Olea-Romacho, JHEP **01**, 133 (2024), 2307.11639.
- [59] A. Salvio, JCAP **12**, 046 (2023), 2307.04694.
- [60] Y. Gouttenoire, Phys. Lett. B **855**, 138800 (2024), 2311.13640.
- [61] M. Arteaga, A. Ghoshal, and A. Strumia (2024), 2409.04545.
- [62] I. K. Banerjee, F. Rescigno, and A. Salvio, JCAP **07**, 007 (2025), 2412.06889.
- [63] I. K. Banerjee, U. K. Dey, and S. Khalil, JHEP **12**, 009 (2024), 2406.12518.
- [64] Q.-H. Cao, M. Tanaka, J.-C. Wang, K.-P. Xie, and J.-J. Zhang (2025), 2505.23007.
- [65] I. Baldes, S. Blasi, A. Mariotti, A. Sevrin, and K. Turbang, Phys. Rev. D **104**, 115029 (2021), 2106.15602.
- [66] P. Huang and K.-P. Xie, JHEP **09**, 052 (2022), 2206.04691.
- [67] E. J. Chun, T. P. Dutka, T. H. Jung, X. Nagels, and M. Vanvlasselaer, JHEP **09**, 164 (2023), 2305.10759.

- [68] L. Chataignier, T. Prokopec, M. G. Schmidt, and B. Świeżewska, *JHEP* **08**, 083 (2018), 1805.09292.
- [69] L. Dolan and R. Jackiw, *Phys. Rev. D* **9**, 3320 (1974).
- [70] A. D. Linde, *Nucl. Phys. B* **216**, 421 (1983), [Erratum: *Nucl.Phys.B* 223, 544 (1983)].
- [71] A. H. Guth and S. H. H. Tye, *Phys. Rev. Lett.* **44**, 631 (1980), [Erratum: *Phys.Rev.Lett.* 44, 963 (1980)].
- [72] A. H. Guth and E. J. Weinberg, *Phys. Rev. D* **23**, 876 (1981).
- [73] M. D. Rintoul and S. Torquato, *Journal of physics a: mathematical and general* **30**, L585 (1997).
- [74] R. D. Pisarski and F. Wilczek, *Phys. Rev. D* **29**, 338 (1984).
- [75] J. Braun and H. Gies, *JHEP* **06**, 024 (2006), hep-ph/0602226.
- [76] Y. Guan and S. Matsuzaki, *JHEP* **09**, 140 (2024), 2405.03265.
- [77] T. P. Dutka, T. H. Jung, and C. S. Shin, *JHEP* **05**, 182 (2025), 2412.15864.
- [78] M. Christiansen, E. Madge, C. Puchades-Ibáñez, M. E. Ramirez-Quezada, and P. Schwaller (2025), 2511.02910.
- [79] J. Liu, R. Qin, and L. Bian (2026), 2601.05793.
- [80] R. Qin and L. Bian, *Phys. Rev. D* **111**, L051702 (2025), 2408.09677.
- [81] W.-Y. Ai, J. Alexandre, and S. Sarkar, *Phys. Rev. D* **109**, 045010 (2024), 2312.04482.
- [82] A. Ekstedt, O. Gould, and J. Hirvonen, *JHEP* **12**, 056 (2023), 2308.15652.
- [83] O. Gould, A. Kormu, and D. J. Weir, *Phys. Rev. D* **111**, L051901 (2025), 2404.01876.
- [84] M. J. Baker, J. Kopp, and A. J. Long, *Phys. Rev. Lett.* **125**, 151102 (2020), 1912.02830.
- [85] D. Chway, T. H. Jung, and C. S. Shin, *Phys. Rev. D* **101**, 095019 (2020), 1912.04238.
- [86] J.-P. Hong, S. Jung, and K.-P. Xie, *Phys. Rev. D* **102**, 075028 (2020), 2008.04430.
- [87] G. Bertone, D. Hooper, and J. Silk, *Phys. Rept.* **405**, 279 (2005), hep-ph/0404175.
- [88] S. Navas et al. (Particle Data Group), *Phys. Rev. D* **110**, 030001 (2024).
- [89] O. Lebedev, A. P. Morais, V. Oliveira, and R. Pasechnik, *JHEP* **04**, 136 (2025), 2410.21874.
- [90] G. Arcadi, D. Cabo-Almeida, and O. Lebedev, *Phys. Lett. B* **861**, 139268 (2025), 2409.02191.
- [91] Y. Bai, M. Korwar, and N. Orlofsky, *JHEP* **07**, 167 (2020), 2005.00503.
- [92] T. W. B. Kibble, *J. Phys. A* **9**, 1387 (1976).
- [93] W. H. Zurek, *Nature* **317**, 505 (1985).
- [94] M. B. Einhorn and K. Sato, *Nucl. Phys. B* **180**, 385 (1981).
- [95] J. Yang, R. Zhou, and L. Bian, *Phys. Lett. B* **839**, 137822 (2023), 2204.07540.
- [96] J. Preskill, *Phys. Rev. Lett.* **43**, 1365 (1979).
- [97] F. Brümmer, G. Ferrante, T. Fischer, and M. Frigerio (2025), 2509.21924.
- [98] R. Aaij et al. (LHCb), *Phys. Rev. Lett.* **115**, 161802 (2015), 1508.04094.
- [99] R. Aaij et al. (LHCb), *Phys. Rev. D* **95**, 071101 (2017), 1612.07818.
- [100] E. Cortina Gil et al. (NA62), *JHEP* **02**, 201 (2021), 2010.07644.
- [101] E. Cortina Gil et al. (NA62), *JHEP* **03**, 058 (2021), 2011.11329.
- [102] M. W. Winkler, *Phys. Rev. D* **99**, 015018 (2019), 1809.01876.
- [103] A. V. Artamonov et al. (BNL-E949), *Phys. Rev. D* **79**, 092004 (2009), 0903.0030.
- [104] S. Foroughi-Abari and A. Ritz, *Phys. Rev. D* **102**, 035015 (2020), 2004.14515.
- [105] P. Abratenko et al. (MicroBooNE), *Phys. Rev. Lett.* **127**, 151803 (2021), 2106.00568.
- [106] J. L. Feng, M. Kaplinghat, H. Tu, and H.-B. Yu, *JCAP* **07**, 004 (2009), 0905.3039.
- [107] P. Agrawal, F.-Y. Cyr-Racine, L. Randall, and J. Scholtz, *JCAP* **05**, 022 (2017), 1610.04611.
- [108] M. Badziak, G. Grilli di Cortona, K. Harigaya, and M. Łukawski, *JHEP* **10**, 057 (2022), 2202.10488.
- [109] J.-H. Liang, Y. Liao, X.-D. Ma, and H.-L. Wang, *Phys. Rev. D* **111**, 095033 (2025), 2501.13501.
- [110] S. Baek, P. Ko, W.-I. Park, and E. Senaha, *JHEP* **05**, 036 (2013), 1212.2131.
- [111] M. Hoferichter, J. Ruiz de Elvira, B. Kubis, and U.-G. Meißner, *Phys. Rev. Lett.* **115**, 092301 (2015), 1506.04142.
- [112] J. Aalbers et al. (LZ), *Phys. Rev. Lett.* **135**, 011802 (2025), 2410.17036.
- [113] Z. Bo et al. (PandaX), *Phys. Rev. Lett.* **134**, 011805 (2025), 2408.00664.
- [114] A. Ariga et al. (FASER), *Phys. Rev. D* **99**, 095011 (2019), 1811.12522.
- [115] V. V. Gligorov, S. Knapen, M. Papucci, and D. J. Robinson, *Phys. Rev. D* **97**, 015023 (2018), 1708.09395.
- [116] C. Ahdida et al. (SHiP), *Eur. Phys. J. C* **81**, 451 (2021), 2011.05115.
- [117] P. Amaro-Seoane et al. (LISA) (2017), 1702.00786.
- [118] J. Crowder and N. J. Cornish, *Phys. Rev. D* **72**, 083005 (2005), gr-qc/0506015.
- [119] C. Caprini et al., *JCAP* **04**, 001 (2016), 1512.06239.
- [120] C. Caprini et al., *JCAP* **03**, 024 (2020), 1910.13125.
- [121] J. Luo et al. (TianQin), *Class. Quant. Grav.* **33**, 035010 (2016), 1512.02076.
- [122] W.-H. Ruan, Z.-K. Guo, R.-G. Cai, and Y.-Z. Zhang, *Int. J. Mod. Phys. A* **35**, 2050075 (2020), 1807.09495.
- [123] A. M. Sirunyan et al. (CMS), *JHEP* **06**, 127 (2018), [Erratum: *JHEP* 03, 128 (2019)], 1804.01939.
- [124] A. Djouadi, *Phys. Rept.* **457**, 1 (2008), hep-ph/0503172.
- [125] M. E. Carrington, *Phys. Rev. D* **45**, 2933 (1992).
- [126] P. Gondolo and G. Gelmini, *Nucl. Phys. B* **360**, 145 (1991).
- [127] N. Arkani-Hamed, D. P. Finkbeiner, T. R. Slatyer, and N. Weiner, *Phys. Rev. D* **79**, 015014 (2009), 0810.0713.